International Journal of Multiphase Flow 70 (2015) 22–34

Contents lists available at ScienceDirect

International Journal of Multiphase Flow

journal homepage: www.elsevier.com/locate/ijmulflow

A numerical method to simulate turbulent cavitating flows

A. Gnanaskandan, K. Mahesh *

University of Minnesota, Aerospace Engineering & Mechanics, USA

ARTICLE INFO

Article history:
Received 20 September 2014
Received in revised form 25 October 2014
Accepted 18 November 2014
Available online 8 December 2014

Keywords:
Finite volume methods
Multiphase flows
Cavitation
Unstructured grids
Characteristic-based filtering

ABSTRACT

The objective of this paper is to develop a numerical method for simulating multiphase cavitating flows on unstructured grids. The multiphase medium is represented using a homogeneous mixture model that assumes thermal equilibrium between the liquid and vapor phases. We develop a predictor–corrector approach to solve the governing Navier–Stokes equations for the liquid/vapor mixture, together with the transport equation for the vapor mass fraction. While a non-dissipative and symmetric scheme is used in the predictor step, a novel characteristic-based filtering scheme with a second order TVD filter is developed for the corrector step to handle shocks and material discontinuities in non-ideal gases and mixtures. Additionally, a sensor based on vapor volume fraction is proposed to localize dissipation to the vicinity of discontinuities. The scheme is first validated for simple one dimensional canonical problems to verify its accuracy in predicting jump conditions across material discontinuities and shocks. It is then applied to two turbulent cavitating flow problems – over a hydrofoil using RANS and over a wedge using LES. Our results show that the simulations are in good agreement with experimental data for the above tested cases, and that the scheme can be successfully applied to both RANS and LES methodologies.

Introduction

Cavitation refers to the formation of vapor when pressure in a liquid drops below vapor pressure. The importance of understanding cavitation lies in its occurrence in a wide variety of applications such as valves, injectors and propulsor blades. The numerical simulation of cavitating flows is inherently challenging since these flows possess a wide range of length and time scales. Additionally, the formation of vapor is often followed by growth of vapor cavities which not only vary in size but also form and collapse at different rates, making their prediction difficult.

The most commonly used physical model to simulate cavitating flows is the homogeneous mixture model. It treats the mixture of water and vapor as a single compressible fluid, and solves a separate transport equation for the mass fraction of vapor (Shin et al., 2003; Kunz et al., 2000; Ahuja et al., 2001; Schnerr et al., 2008; Liu et al., 2004; Saito et al., 2007; Seo and Lele, 2009; Seo et al., 2008; Singhal et al., 2002; Senocak and Shyy, 2002; Adams and Schmidt, 2013; Schmidt et al., 2009). The key differences between commonly used physical models lie in the constitutive equation of state and the mass transfer model. Frikha et al. (2008) provide a review of the different mass transfer models used. Almost all of the simulations mentioned above have used the RANS methodology. However in recent times, DES and LES are also being considered as viable options (Arndt et al., 2000; Bensow and Bark, 2010; Dittakavi et al., 2010; Kinzel et al., 2007; Ji et al., 2013; Wang and Ostoja-Starzewski, 2007). Also, most past simulations invoke the isothermal assumption for cavitation in water. It is known that this assumption is not valid for thermosensitive fluids like cryogenic fluids where an energy equation needs to be solved (Hosangadi and Ahuja, 2005; Zhang et al., 2008; Goncalvès and Patella, 2010). In this study, we use the homogeneous mixture approach with a non-barotropic equation of state for water. In order to maintain a general framework, we have solved an energy equation. In the current investigation, we have focused on hydrodynamic cavitation. The method however, can be applied to thermosensitive fluids as well. The latent heat of evaporation is not considered in this study. Although the specific latent heat of evaporation varies from low values near the critical point to appreciable values near 1 atm and 25 °C, the mass of vapor produced by cavitation is small with respect to the mass of liquid; the amount of latent heat absorbed by vapor formation is therefore negligible. In the examples considered, the vapor mass fraction does not exceed 0.0003.

A turbulent cavitating flow has a broadband spectrum which requires non dissipative numerical schemes (Mahesh et al., 2004; Hou et al., 2005) to represent small scales accurately. However, non-dissipative schemes can become unstable at high Reynolds

* Corresponding author at: 107 Akerman Hall, 110 Union Street, Minneapolis, Minnesota 55455-0153, USA. Tel.: +1 612 624 4175.
E-mail address: kmahesh@aem.umn.edu (K. Mahesh).

http://dx.doi.org/10.1016/j.ijmultiphaseflow.2014.11.009
0301-9322/

numbers. Furthermore, cavitation is characterized by large gradients in density and strong pressure waves formed during vapor cloud collapse. Accurate representation of turbulence in the presence of these strong gradients is a significant challenge and requires appropriate discontinuity capturing methods. Classical monotonic discontinuity-capturing methods are too dissipative and not suitable for turbulent simulations. Modern discontinuity capturing methods like total variation diminishing (TVD) schemes, essentially non-oscillatory (ENO) schemes and monotone upstream-centered schemes for conservation laws (MUSCL) typically incur higher computational cost for achieving higher order of accuracy in the vicinity of discontinuities. Further, these schemes require special treatment near boundaries (Yee et al., 1999). Yee et al. (1999) proposed a class of filters called 'characteristic filters', that add the dissipative part of a traditional shock capturing method to a non-dissipative base scheme. They developed this method for ideal gases on structured grids; Park and Mahesh (2007) proposed an extension to unstructured grids. Numerical boundary conditions for these filters can be same as the existing base schemes, which is an added advantage. Further, the characteristic filter can be applied to the solution once, after a full time step, and hence is considerably cheaper than the TVD, ENO and MUSCL schemes (Lo et al., 2010). A simple linear filter was first proposed by Gustafsson and Olsson (1995), which provides a linear second order dissipation. Yee et al. (1999) then used a second order non-linear TVD filter that takes into account the different wave characteristics of the Euler equations. Both lower order TVD or higher order ENO/WENO type terms can be used as characteristic filters. Lo et al. (2010) observed that WENO type filters perform marginally better than lower order TVD filters and also found WENO type filters to be insensitive to the tunable parameters that appear in the shock capturing scheme. Both Park and Mahesh (2007) and Lo et al. (2010) observed that the original combination of TVD filter and Harten's artificial compression method (ACM) switch (Harten, 1983) proposed by Yee et al. (1999) was not able to distinguish between turbulent fluctuations and shocks, and hence proposed modified switch terms.

In this paper, we extend the characteristic based filtering method to non ideal gases and a mixture of fluids to simulate multiphase cavitating flows on unstructured grids. A predictor–corrector method is used where the predictor step is non-dissipative and the corrector step computes the jump conditions across the discontinuities. The dissipation is spatially localized to reduce dissipation away from the discontinuities. We propose an additional modification to this localization term applicable in multiphase flows. The governing equations are spatially Favre filtered for LES. The additional terms arising out of spatial filtering are modeled using a Dynamic Smagorinsky model. The paper is organized as follows. Section 'Governing equations' outlines the governing equations along with the source terms for evaporation of water and condensation of vapor. Section 'Numerical method' discusses the predictor–corrector algorithm along with the spatial and temporal discretization schemes. The characteristic based filtering applied as a corrector step is also discussed in this section. Validation simulations are presented in Section 'Results', and a brief summary in Section 'Summary' concludes the paper.

Governing equations

We use a homogeneous mixture model that assumes thermal and mechanical equilibrium between the phases i.e. there is no slip velocity or temperature difference between the phases. Also, surface tension effects are ignored. The constituent phases are treated as a single compressible fluid whose density

$$\rho = \rho_l(1-\alpha) + \rho_g\alpha, \tag{1}$$

where ρ_l is the density of liquid and ρ_g is the density of vapor. α is the vapor volume fraction which is related to the vapor mass fraction (Y) by

$$\rho_l(1-\alpha) = \rho(1-Y) \quad \text{and} \quad \rho_g\alpha = \rho Y. \tag{2}$$

The governing equations are the Navier–Stokes equations along with a transport equation for the mass fraction of vapor:

$$\begin{aligned}
\frac{\partial \rho}{\partial t} &= -\frac{\partial}{\partial x_k}(\rho u_k),\\
\frac{\partial \rho u_i}{\partial t} &= -\frac{\partial}{\partial x_k}(\rho u_i u_k + p\delta_{ik} - \sigma_{ik}),\\
\frac{\partial \rho Y}{\partial t} &= -\frac{\partial}{\partial x_k}(\rho Y u_k) + S_e - S_c,
\end{aligned} \tag{3}$$

where ρ, u_i and p are density, velocity and pressure respectively of the mixture. For energy transport, both total energy and internal energy forms are considered. Their relative merits and demerits are discussed in Section 'Multiphase non cavitating shock tube'. The internal energy form is used for the results shown unless specified otherwise.

$$\begin{aligned}
\frac{\partial E_T}{\partial t} &= -\frac{\partial}{\partial x_k}\{(E_T + p)u_k - \sigma_{ik}u_i - Q_k\},\\
\frac{\partial \rho e_s}{\partial t} &= -\frac{\partial}{\partial x_k}(\rho e_s u_k - Q_k) - p\frac{\partial u_k}{\partial x_k} + \sigma_{ik}\frac{\partial u_i}{\partial x_k}.
\end{aligned} \tag{4}$$

Here E_T and e_s are total energy and internal energy respectively.

$$\begin{aligned}
&\rho e_s = \rho_l e_l(1-\alpha) + \rho_g e_g \alpha, \text{ where}\\
&e_l = C_{vl}T + \frac{P_c}{\rho_l},\\
&e_g = C_{vg}T,\\
&\rho e_s = \rho C_{vm}T + \rho(1-Y)\frac{P_c K_l}{p+P_c} \text{ and}\\
&E_T = \rho e_s + \frac{1}{2}\rho u_k u_k.
\end{aligned} \tag{5}$$

Here, e_l and e_g are the internal energies of liquid and gas respectively. C_{vl} and C_{vg} are the specific heats at constant volume for liquid and vapor respectively and C_{pl} and C_{pg} are the specific heats at constant pressure. The system is closed using a mixture equation of state based on stiffened equation of state for water and ideal gas equation for vapor.

$$p = Y\rho R_g T + (1-Y)\rho K_l T\frac{p}{p+P_c}. \tag{6}$$

Here, R_g = 461.6 J/Kg K, K_l = 2684.075 J/Kg K and $P_c = 786.333 \times 10^6$ are constants associated with the equation of state of vapor and liquid. The density and speed of sound predicted by the stiffened equation of state is compared with the National Institute of Standards and Technology (NIST) data in Fig. 1(a) and a good agreement is observed. However the stiffened equation of state underpredicts the value of specific heat at constant volume C_{vl} (predicts it to be 1500.3 J/Kg K as opposed to the NIST value of 4157.4 J/Kg K). This is not seen as a serious drawback in the current study because, heat transfer effects within the liquid phase are small in hydrodynamic cavitation at ambient pressure and temperature. The proposed numerical method however can be applied to more complicated equations of state for water like the Tait equation of state. The stiffened equation of state is chosen due to its simplicity. Since internal energy is a function of both pressure and temperature, we need to obtain these variables using Eqs. (5) and (6). Solving these two equations simultaneously yields a quadratic equation $ap^2 + bp + c = 0$, where

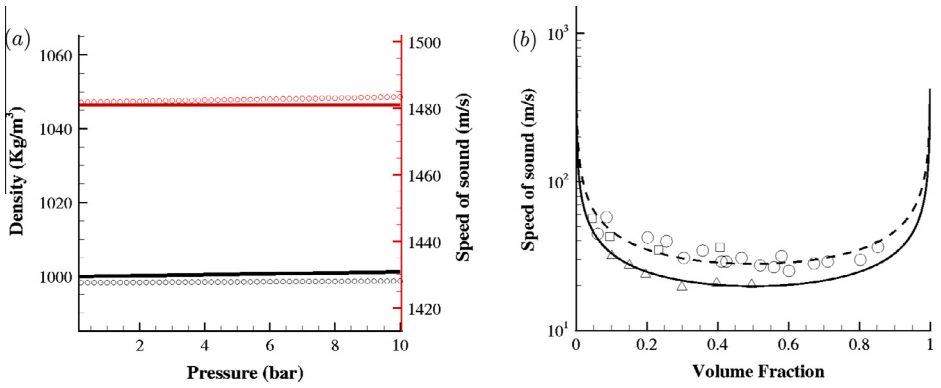

Fig. 1. (a) Comparison of density and speed of sound in water with NIST data, ○ : NIST data, — : Present. (b) Comparison of speed of sound in water–air mixture to experiment, □: Henry et al. (1971), ○ : Semenov and Kosterin (1964), △ : Karplus (1957), — : Present (0.1 MPa), – – – – : Present (0.2 MPa).

$$
\begin{aligned}
&a = C_{vm},\\
&b = C_{vm}P_c + (1-Y)P_cK_l - [(1-Y)K_l + YR_g]\rho e_s \text{ and}\\
&c = -YR_gP_c\rho e_s.
\end{aligned}
\tag{7}
$$

The pressure is obtained as the positive root of this quadratic equation and temperature is then computed from either Eq. (5) or Eq. (6). The viscous stress σ_{ij} and heat flux Q_i are given by

$$
\begin{aligned}
&\sigma_{ij} = \mu\left(\frac{\partial u_i}{\partial x_j} + \frac{\partial u_j}{\partial x_i} - \frac{2}{3}\frac{\partial u_k}{\partial x_k}\delta_{ij}\right) \text{ and}\\
&Q_i = k\frac{\partial T}{\partial x_i},
\end{aligned}
\tag{8}
$$

where the mixture viscosity and mixture thermal conductivity are defined as

$$
\begin{aligned}
&\mu = \mu_l(1-\alpha)(1+2.5\alpha) + \mu_g\alpha \text{ and}\\
&k = k_l(1-\alpha) + k_g\alpha.
\end{aligned}
\tag{9}
$$

To perform LES, Eq. (3) are first Favre filtered spatially:

$$
\begin{aligned}
&\frac{\partial\overline{\rho}}{\partial t} = -\frac{\partial}{\partial x_k}(\overline{\rho}\tilde{u}_k),\\
&\frac{\partial\overline{\rho}\tilde{u}_i}{\partial t} = -\frac{\partial}{\partial x_k}(\overline{\rho}\tilde{u}_i\tilde{u}_k + \overline{p}\delta_{ik} - \tilde{\sigma}_{ik} - \tau_{ik}),\\
&\frac{\partial\overline{\rho}\widetilde{Y}}{\partial t} = -\frac{\partial}{\partial x_k}\left(\overline{\rho}\widetilde{Y}\tilde{u}_k - t_k\right) + \tilde{S}_e - \tilde{S}_c,\\
&\frac{\partial\overline{\rho}\tilde{e}_s}{\partial t} = -\frac{\partial}{\partial x_k}\left(\overline{\rho}\tilde{e}_s\tilde{u}_k - \tilde{Q}_k - q_k\right) - \overline{p}\frac{\partial\tilde{u}_k}{\partial x_k} + \tilde{\sigma}_{ik}\frac{\partial\tilde{u}_i}{\partial x_k}.
\end{aligned}
\tag{10}
$$

Here, the tilde quantities are Favre averaged quantities and τ_{ik}, q_k and t_k are subgrid scale (SGS) terms namely: SGS stress, SGS heat flux and SGS scalar flux. These terms are modeled using the Dynamic Smagorinsky model (DSM) (Germano et al., 1991):

$$
\begin{aligned}
&\tau_{ij} - \frac{\delta_{ij}}{3}\tau_{kk} = -2C_S(\mathbf{x},t)\overline{\rho}\Delta^2\left|\widetilde{S}\right|\widetilde{S_{ij}^*},\\
&\tau_{kk} = 2C_I(\mathbf{x},t)\overline{\rho}\Delta^2\left|\widetilde{S}\right|^2,\\
&q_i = -\overline{\rho}\frac{C_S(\mathbf{x},t)\Delta^2\left|\widetilde{S}\right|}{Pr_T}\frac{\partial\overline{T}}{\partial x_i},\\
&t_i = -\overline{\rho}\frac{C_S(\mathbf{x},t)\Delta^2\left|\widetilde{S}\right|}{Sc_T}\frac{\partial\overline{Y}}{\partial x_i},
\end{aligned}
\tag{11}
$$

where $|S| = \sqrt{2S_{ij}S_{ij}}$ and $S_{ij}^* = S_{ij} - 1/3S_{kk}\delta_{ij}$. The model coefficients C_s, C_I, Pr_T and Sc_T are determined by the Germano identity (Germano et al., 1991). For example,

$$
\begin{aligned}
&C_S\Delta^2 = \frac{1}{2}\frac{\left\langle L_{ij}^*M_{ij}^*\right\rangle}{\left\langle M_{ij}^*M_{ij}^*\right\rangle},\\
&L_{ij}^* = \left(\frac{\widehat{\overline{\rho}\tilde{u}_i\cdot\overline{\rho}\tilde{u}_j}}{\overline{\rho}}\right) - \frac{\widehat{\overline{\rho}\tilde{u}_i}\cdot\widehat{\overline{\rho}\tilde{u}_j}}{\widehat{\overline{\rho}}},\\
&M_{ij}^* = \overline{\rho}\widehat{\left|\widetilde{S}\right|\widetilde{S_{ij}^*}} - \widehat{\overline{\rho}}\left(\frac{\widehat{\Delta}}{\Delta}\right)^2\widehat{\left|\widetilde{S}\right|}\,\widehat{\widetilde{S_{ij}^*}},
\end{aligned}
\tag{12}
$$

where, $\langle\cdot\rangle$ denotes spatial average over homogeneous direction(s) and the caret denotes test filtering. Test filtering is defined by the linear interpolation from face values of a control volume, which is again the interpolation from two adjacent cell center values (Park and Mahesh, 2007):

$$
\widehat{\phi} = \frac{1}{N_{\text{face}}}\sum_{\text{no of face}}\phi_f = \frac{1}{2N_{\text{face}}}\sum_{\text{no of face}}(\phi_{icv1} + \phi_{icv2}),
\tag{13}
$$

where N_{face} is the number of faces for a given control volume.

Speed of sound

The expression for the speed of sound in a liquid–gas mixture is obtained using the equation of state and Gibbs equation and is given by

$$
\begin{aligned}
&a^2 = \frac{C_1T}{C_0 - \frac{C_1}{C_{pm}}}, \text{ where}\\
&C_0 = 1 - (1-Y)\rho K_lT\frac{P_c}{(p+P_c)^2},\\
&C_1 = R_gY - K_l(1-Y)\frac{p}{p+P_c} \text{ and}\\
&C_{pm} = YC_{pg} + (1-Y)C_{pl}.
\end{aligned}
\tag{14}
$$

The change in speed of sound with gas volume fraction at given temperature and pressure obtained using the above relation, is compared to experimental results (Henry et al., 1971; Semenov and Kosterin, 1964; Karplus, 1957) in Fig. 1(b). This sound speed is obtained assuming that there is no mass transfer between the phases and hence is the non-equilibrium sound speed. Note the good agreement with experiments; also the effect of gas volume fraction in changing the acoustic characteristics of water is evident. Note that the sound speed in the mixture ranges from 1480 m/s for pure water to 30 m/s for certain values of gas volume fraction.

Cavitation source terms

In case of cavitating flows, S_e and S_c are source terms for evaporation of water and condensation of vapor and are given by

$$S_e = C_e \alpha^2 (1-\alpha)^2 \frac{\rho_l}{\rho_g} \frac{\max((p_v - p), 0)}{\sqrt{2\pi R_g T}}, \tag{15}$$
$$S_c = C_c \alpha^2 (1-\alpha)^2 \frac{\max((p_v - p), 0)}{\sqrt{2\pi R_g T}},$$

where α is the volume fraction of vapor and p_v is the vapor pressure. C_e and C_c are empirical constants. Saito et al. (2007) have shown that the source terms are not very sensitive to the values of these empirical constants and arrive at an optimum value of 0.1 for both the constants. Vapor pressure is related to temperature by

$$p_v = p_k \exp\left(\left(1 - \frac{T_k}{T}\right)(a + (b - cT)(T - d)^2)\right), \tag{16}$$

where $p_k = 22.130$ MPa, $T_k = 647.31$ K, $a = 7.21$, $b = 1.152 \times 10^{-5}$, $c = -4.787 \times 10^{-9}$, $d = 483.16$.

Numerical method

The numerical method adopts a novel predictor corrector approach. In the predictor step, Eq. (3) are discretized using a collocated, cell-centered finite volume method. Fig. 2(a) illustrates the storage of variables and the notation used. The solution is first advanced using a non-dissipative predictor step. The characteristic based filter is then applied as a corrector.

Predictor step

A predicted value is first obtained by solving Eq. (3) using a symmetric and non-dissipative scheme. The convective fluxes at the face are estimated using a symmetric average with a gradient term using Taylor series expansion to obtain

$$\phi_{f_c} = \frac{\phi_{icv1} + \phi_{icv2}}{2} + \frac{1}{2}\left(\nabla\phi|_{icv1} \cdot \Delta\mathbf{x}^{icv1} + \nabla\phi|_{icv2} \cdot \Delta\mathbf{x}^{icv2}\right), \tag{17}$$

where $\Delta\mathbf{x}^{icv1} = \mathbf{x}_{\mathbf{f_c}} - \mathbf{x}_{icv1}$, and $\nabla\phi|_{icv1}$ denotes the gradient defined at $icv1$. The viscous term is split into two parts, $\sigma_{ij} = \sigma^1_{ij} + \sigma^2_{ij}$, where $\sigma^1_{ij} = \frac{\mu}{Re}\frac{\partial u_i}{\partial x_j}$ and $\sigma^2_{ij} = \frac{\mu}{Re}\left(\frac{\partial u_j}{\partial x_i} - \frac{2}{3}\frac{\partial u_k}{\partial x_k}\delta_{ij}\right)$. σ^2_{ij} can be interpreted as a 'compressible' contribution, since it vanishes in the incompressible limit. The 'incompressible' component σ^1_{ij} is computed by

$$\frac{1}{V_{cv}}\sum_{\text{faces}}\left(\frac{\mu}{Re}\right)_f \left.\frac{\partial u_i}{\partial x_j}\right|_f n_j A_f = \frac{1}{V_{cv}}\sum_{\text{faces}}\left(\frac{\mu}{Re}\right)_f \left.\frac{\partial u_i}{\partial n}\right|_f A_f. \tag{18}$$

Here, the normal gradient at the face is computed by

$$\frac{\partial\phi}{\partial n} = \frac{\phi_{ifn2} - \phi_{ifn1}}{d_f}, \tag{19}$$

where $ifn1$ ($ifn2$) is the projection of $icv1$ ($icv2$) onto the extension of normal vector $\mathbf{n}$ and d_f is the distance between $ifn1$ and $ifn2$ as illustrated in Fig. 2(b). ϕ_{ifn1} is given by

$$\phi_{ifn1} = \phi_{icv1} + \nabla\phi|_{icv1} \cdot (\mathbf{x}_{ifn1} - \mathbf{x}_{icv1}), \tag{20}$$

where the linear least-square method is used to determine the gradient $\nabla\phi$ at $icv1$. Viscosity at the cell face is obtained using Eq. (17) and a least square reconstruction. Thus, the incompressible part corresponds to a compact-stencil method. $\sigma^2_{ij,f}$ is constructed by the interpolation of $\sigma^2_{ij}\big|_{icv1}$ and $\sigma^2_{ij}\big|_{icv2}$ using Eq. (17).

Discrete positivity of viscous dissipation

The viscous term in the internal energy equation corresponds to the viscous dissipation term and by the second law of thermodynamics, should always remain positive. This term is therefore re-written to discretely ensure positivity. Note that

$$\sigma_{ik}\frac{\partial u_i}{\partial x_k} = \begin{pmatrix} \frac{4\partial u}{3\partial x} & \frac{\partial u}{\partial y}+\frac{\partial v}{\partial x} & \frac{\partial u}{\partial z}+\frac{\partial w}{\partial x} \\ \frac{\partial u}{\partial y}+\frac{\partial v}{\partial x} & \frac{4\partial v}{3\partial y} & \frac{\partial v}{\partial z}+\frac{\partial w}{\partial y} \\ \frac{\partial u}{\partial z}+\frac{\partial w}{\partial x} & \frac{\partial v}{\partial z}+\frac{\partial w}{\partial y} & \frac{4\partial w}{3\partial z} \end{pmatrix} \begin{pmatrix} \frac{\partial u}{\partial x} & \frac{\partial u}{\partial y} & \frac{\partial u}{\partial z} \\ \frac{\partial v}{\partial x} & \frac{\partial v}{\partial y} & \frac{\partial v}{\partial z} \\ \frac{\partial w}{\partial x} & \frac{\partial w}{\partial y} & \frac{\partial w}{\partial z} \end{pmatrix}$$

can be re-written as

$$\sigma_{ik}\frac{\partial u_i}{\partial x_k} = \frac{4}{3}\left[\left(\frac{\partial u}{\partial x}\right)^2 + \left(\frac{\partial v}{\partial y}\right)^2 + \left(\frac{\partial w}{\partial z}\right)^2\right] + \left(\frac{\partial u}{\partial y} + \frac{\partial v}{\partial x}\right)^2 + \left(\frac{\partial u}{\partial z} + \frac{\partial w}{\partial x}\right)^2 + \left(\frac{\partial v}{\partial z} + \frac{\partial w}{\partial y}\right)^2. \tag{21}$$

This sum of squares is strictly positive and hence viscous dissipation remains discretely positive at all times. Eq. (21) also has fewer operation counts when compared to computing the scalar product of two tensors.

Time advancement

Two time advancement schemes are implemented: a second-order explicit Adams–Bashforth scheme and a second order segregated implicit Crank–Nicholson scheme. For the Adams–Bashforth scheme,

$$q_j^{n+1} = q_j^n + \frac{\Delta t}{2}\left[3\text{rhs}_j(\mathbf{q}^n) - \text{rhs}_j(\mathbf{q}^{n-1})\right], \tag{22}$$

where rhs_j denotes jth component of the right hand side of the governing equation, and the superscript n denotes the nth time step. In the segregated implicit method, the governing equations are discretized using the Crank–Nicholson method. For example, the discrete continuity equation is

$$\frac{\rho_{cv}^{n+1} - \rho_{cv}^n}{\Delta t} V_{cv} = -\frac{1}{2}\sum_{\text{faces}}(\rho V_N)_f^n A_f - \frac{1}{2}\sum_{\text{faces}}(\rho V_N)_f^{n+1} A_f. \tag{23}$$

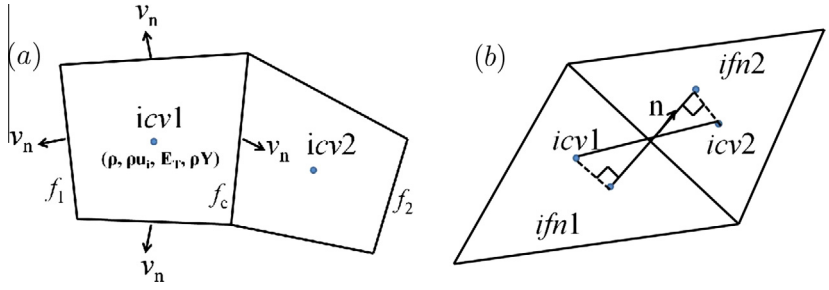

Fig. 2. (a) Schematic of the collocated finite volume method. (b) Schematic for computation of face normal gradient for viscous terms.

The face value can be written as the sum of the neighboring control volume values as $\rho_f = \frac{\rho_{cv}+\rho_{nbr}}{2}$. On rearrangement,

$$\rho_{cv}^{n+1}\left[1+\frac{\Delta t}{4V_{cv}}\sum_{\text{faces}}V_{N_f}^{n+1,k}A_f\right]+\left[\frac{\Delta t}{4V_{cv}}\sum_{\text{faces}}\rho_{nbr}^{n+1}V_{N_f}^{n+1,k}A_f\right] = -\left[\frac{\Delta t}{2V_{cv}}\sum_{\text{faces}}\rho_f^n V_{N_f}^n A_f\right]. \tag{24}$$

The above equation is solved iteratively to obtain an estimate for $\rho^{n+1,k}$ for all the control volumes, where k is the outer loop variable. The other equations are solved similarly to obtain $\rho u_i^{n+1,k}$, $\rho e_s^{n+1,k}$ and $\rho Y^{n+1,k}$ for all the control volumes. This step is repeated until the difference between $(k+1)^{\text{th}}$ time variables and k^{th} time variables becomes negligible, thus coupling the equations using an outer iteration. All results presented in this paper use explicit time advancement.

Corrector step: characteristic-based Filter

The predictor step described in the previous section does not explicitly add dissipation and hence cannot capture discontinuities (both shocks and material discontinuities). An external discontinuity capturing mechanism is therefore provided. Yee et al. (1999) developed a characteristic based filtering method for ideal gases on structured grids which was extended to ideal gases on unstructured grids by Park and Mahesh (2007). In this paper, a characteristic based filtering method is developed for mixtures of fluids and non ideal gases on unstructured grids. Note that any time integration scheme can be used in the predictor step and it will not affect the implementation of the corrector step. Once a physical time step Δt is advanced to obtain the solution $\widehat{q}^{n+1}$ from q^n, the final solution q^{n+1} at $t+\Delta t$ is obtained from a corrector scheme

$$q_{cv}^{n+1} = \widehat{q}_{cv}^{n+1} - \frac{\Delta t}{V_{cv}}\sum_{\text{faces}}(F_f^*.n_f)A_f, \tag{25}$$

where F_f^* is the filter numerical flux of the following form

$$F_{fc}^* = \frac{1}{2}R_{fc}\Phi_{fc}^*. \tag{26}$$

Here R_{fc} is the right eigenvector vector at the face computed using Roe-average of the variables from left and right control volumes. The expression for the lth component of Φ^*, ϕ^{*l} is given by

$$\phi_{fc}^{*l} = k\theta_{fc}^l\phi_{fc}^l, \tag{27}$$

where k is an adjustable parameter. The value of k is problem dependent and its effect on the results is demonstrated in Section 'One dimensional cavitating tube'. θ_{fc} is the Harten's switch function given by

$$\theta_{fc} = \sqrt{0.5(\widehat{\theta}_{icv1}^2+\widehat{\theta}_{icv2}^2)},\quad \widehat{\theta}_{icv1} = \frac{|\beta_{fc}|-|\beta_{f1}|}{|\beta_{fc}|+|\beta_{f1}|},\quad \widehat{\theta}_{icv2} = \frac{|\beta_{f2}|-|\beta_{fc}|}{|\beta_{f2}|+|\beta_{fc}|}. \tag{28}$$

Here, $\beta_f = R_f^{-1}(q_{icv2}-q_{icv1})$ is the difference between characteristic variables across the face. f_1 and f_2 in a structured grid are the face neighbors in the corresponding direction (i.e. in the direction of the face normal). This definition is not possible in an unstructured grid, hence the concept of most parallel faces was introduced in Park and Mahesh (2007). Fig. 2(a) illustrates this concept. For ϕ^ℓ, the Harten-Yee TVD form is used as suggested by Yee et al. (1999).

$$\phi_{f_c}^\ell = \frac{1}{2}\Psi\left(a_{f_c}^\ell\right)\left(g_{icv1}^\ell+g_{icv2}^\ell\right)-\Psi\left(a_{f_c}^\ell+\gamma_{f_c}^\ell\right)\beta_{f_c}^\ell,\quad \gamma_{f_c}^\ell = \frac{1}{2}\frac{\Psi\left(a_{f_c}^\ell\right)\left(g_{icv2}^\ell-g_{icv1}^\ell\right)\beta_{f_c}^\ell}{\left(\beta_{f_c}^\ell\right)^2+\epsilon}, \tag{29}$$

where $\epsilon = 10^{-7}$ and $\Psi(z) = \sqrt{\delta+z^2}$. $\delta = 1/16$ is introduced for the entropy fixing (Yee et al., 1999). $a_{f_c}^\ell$ is the element of the jacobian matrix. For a structured grid, the value of the limiter function g_{icv} can be defined at the cell centers using the value of α at faces. Defining this in an unstructured grid will require interpolation. To avoid this, we define g at the faces. This is more natural because Eq. (29) require only symmetric average $\frac{1}{2}(g_{icv1}+g_{icv2})$ and difference $\frac{1}{2}(g_{icv2}-g_{icv1})$ of g between the neighboring control volumes. Thus the expression of g is given by

$$g_{f_c}^{+\ell} \equiv \frac{1}{2}\left\{\text{minmod}\left(\beta_{f_1}^\ell,\beta_{f_c}^\ell\right)+\text{minmod}\left(\beta_{f_c}^\ell,\beta_{f_2}^\ell\right)\right\},\quad g_{f_c}^{-\ell} \equiv \frac{1}{2}\left\{\text{minmod}\left(\beta_{f_2}^\ell,\beta_{f_c}^\ell\right)-\text{minmod}\left(\beta_{f_1}^\ell,\beta_{f_c}^\ell\right)\right\}. \tag{30}$$

The expressions for $\phi_{f_c}^\ell$ and $\gamma_{f_c}^\ell$ can now be written as

$$\phi_{f_c}^\ell = \Psi\left(a_{f_c}^\ell\right)g_{f_c}^{+\ell}-\Psi\left(a_{f_c}^\ell+\gamma_{f_c}^\ell\right)\beta_{f_c}^\ell,\quad \gamma_{f_c}^\ell = \frac{\Psi\left(a_{f_c}^\ell\right)g_{f_c}^{-\ell}\beta_{f_c}^\ell}{\left(\beta_{f_c}^\ell\right)^2+\epsilon}, \tag{31}$$

This approach avoids any interpolation between cell center and faces and hence, on Cartesian grids will be equivalent to the expression proposed for structured grids by Yee et al. (1999). In order to determine the eigenvectors of the system, the flux Jacobian matrix needs to be computed. First the expression for pressure needs to be expressed in terms of solution variables $q_j = (\rho, \rho u_i, \rho E_T, \rho Y)$. Note that total energy is used here even though internal energy is solved in the predictor step, since jump conditions need to be obtained for conservative variables. Eq. (7), when expressed in terms of the solution variables q becomes

$$a = C_{vl}(q_1-q_6)+C_{vg}q_6,\quad b = C_{pl}P_c(q_1-q_6)+C_{vg}P_cq_6-[(q_1-q_6)K_l+q_6R_g]\left[q_5-0.5\frac{q_2{}^2+q_3^2+q_4^2}{q_1}\right]\text{ and}\quad c = -q_6R_gP_c\left[q_5-0.5\frac{q_2{}^2+q_3^2+q_4^2}{q_1}\right]. \tag{32}$$

$\frac{\partial p}{\partial q_j}$ is then obtained as

$$\frac{\partial p}{\partial q_j} = -\frac{\left[p^2\frac{\partial a}{\partial q_j}+p\frac{\partial b}{\partial q_j}+\frac{\partial c}{\partial q_j}\right]}{2ap+b}. \tag{33}$$

Once the flux Jacobian matrix is obtained, the eigenvector vector matrix R_{ij} and its inverse R_{ij}^{-1} can be evaluated.

Modification of Harten's switch

Yee et al. (1999) made use of Harten's switch θ_{fc} to spatially localize the dissipation. Park and Mahesh (2007) showed that for a single phase flow, θ_{fc} proposed by Yee et al. is excessively dissipative. They make use of a temporally decaying isotropic turbulence problem to show that θ_{fc} affects resolved turbulence, and propose a modified localization term based on divergence and vorticity (Ducros et al., 1999). In order to evaluate the performance of this term and the Harten's switch in multiphase flows, we perform LES of decaying isotropic turbulence in a mixture of water and vapor. The simulation is performed on a coarse grid of 32^3 volumes with an initial Taylor micro scale Reynolds number $Re_\lambda = u_{rms}\lambda/\nu = 68.7$. The initial spectrum is given by

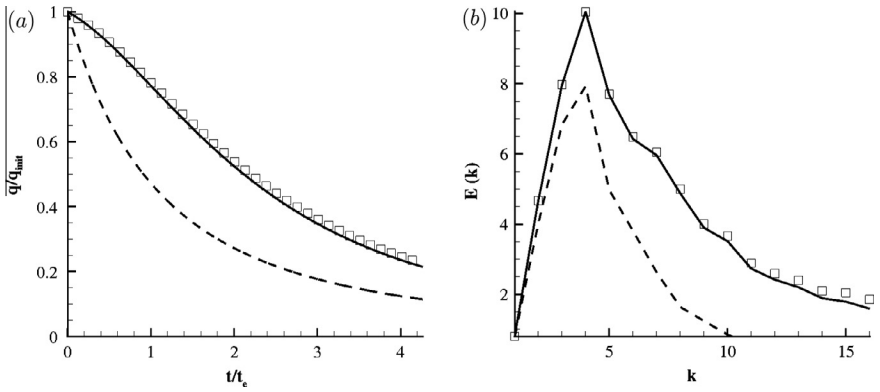

Fig. 3. (a) Comparison of temporal decay of kinetic energy obtained using original Harten's switch and modified singlephase switch to results obtained using no shock capturing. (b) Radial energy spectrum at $t/t_e = 4.0$ obtained using original Harten's switch and modified singlephase switch compared to results obtained using no shock capturing. □: No shock capturing, ———— : Harten's switch, —— : Modified switch.

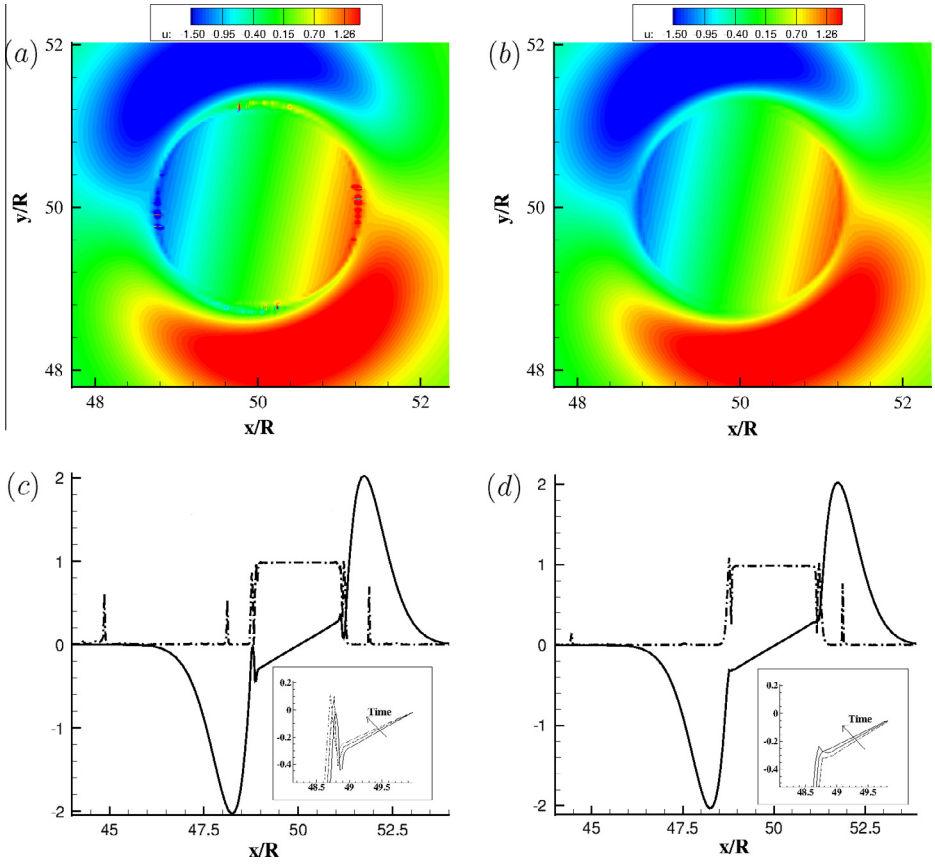

Fig. 4. (a) and (b) Streamwise velocity contours for modified single phase and multiphase switch respectively. (c) Variation of modified singlephase switch and v-velocity along the $\theta = 0$ line. (d) Variation of modified multiphase switch and v-velocity along the $\theta = 0$ line. —— : V-velocity, ———— : Switch.

$$E(k) = 16\sqrt{\frac{2}{\pi}}\frac{u_0^2}{k_0}\left(\frac{k}{k_0}\right)^4 \exp\left(-2k^2/k_0^2\right), \tag{34}$$

and the initial fluctuation Mach number is 0.001. The pressure fluctuations are such that the flow does not cavitate. Even in the absence of any discontinuities, the result is found to be dissipative thereby affecting the resolved turbulence as shown in Fig. 3. Hence θ_{f_c} is modified using a sensor based on Ducros et al. (1999) to prevent excessive dissipation.

$$\begin{aligned}
\theta_{f_c} &= \theta_{f_c}\theta^{\star}_{f_c},\\
\theta^{\star}_{f_c} &= \frac{1}{2}\left(\theta^{\star}_{icv1} + \theta^{\star}_{icv2}\right),\\
\theta^{\star}_{icv1} &= \frac{(\nabla\cdot\mathbf{u})^2_{icv1}}{(\nabla\cdot\mathbf{u})^2_{icv1} + \Omega^2_{icv1} + \epsilon}.
\end{aligned} \tag{35}$$

Here Ω is the vorticity magnitude and $\epsilon = 10^{-7}$ is a small positive value. The modified term, henceforth called as modified single phase switch, limits dissipation away from discontinuities. This is

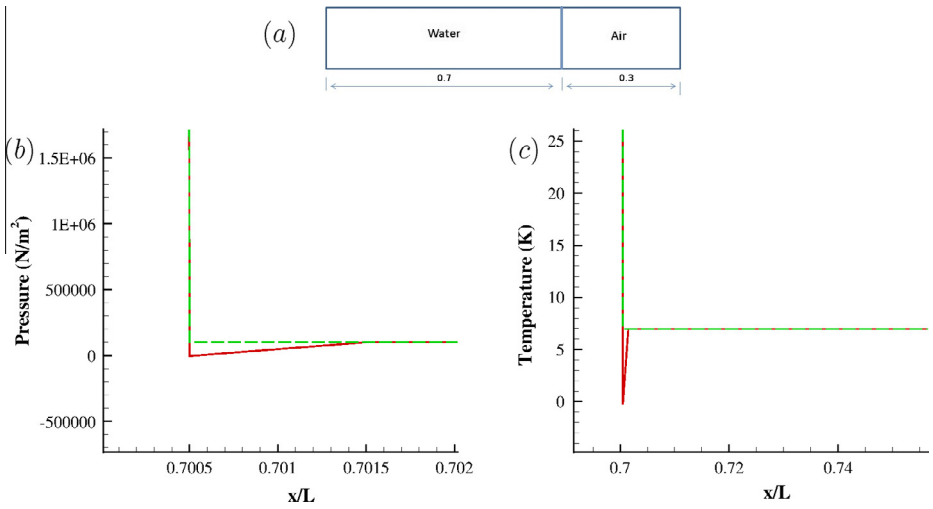

Fig. 5. (a) Schematic for air–water shock tube. (b) Variation of pressure after the first time step. (c) Variation of temperature after the first time step. (—): Total energy form, (···): Internal energy form.

clearly seen in Fig. 3 which shows kinetic energy (q) decay and the radial energy spectrum. t_e is the eddy turnover time.

However, even this modification causes problems in a cavitating flow. Consider an inviscid cavitating vortex on a square domain of dimensions 100R x 100R. The initial velocity field is

$$u = -\frac{C(y-y_c)}{R^2}\exp(-r^2/2) \text{ and}$$
$$v = \frac{C(x-x_c)}{R^2}\exp(-r^2/2). \tag{36}$$

Here $r^2 = ((x-x_c)^2 + (y-y_c)^2)/R^2$ and $R = 1, C = 5.0, x_c = y_c = 50R$. Constant density, pressure and temperature are specified initially. As the solution evolves, pressure in the center of the vortex drops below vapor pressure and the flow cavitates. As the vortex cavitates, the value of the modified singlephase switch becomes very small because of the large vorticity there. Hence numerical oscillations are encountered as shown in Fig. 4(a). Fig. 4(c) shows the variation of v-velocity and the modified singlephase switch along the $\theta = 0$ line. Note the oscillation in v-velocity and the very small value of the switch at the corresponding location. This oscillation increases with time and causes the solution to become unstable. As a remedy, an additional term is added to the modified single phase switch.

$$\theta^{\star}_{f_c} = \frac{1}{2}\left(\theta^{\star}_{ic\nu 1} + \theta^{\star}_{ic\nu 2}\right) + \left|\left(\alpha_{ic\nu 2} - \alpha_{ic\nu 1}\right)\right| \tag{37}$$

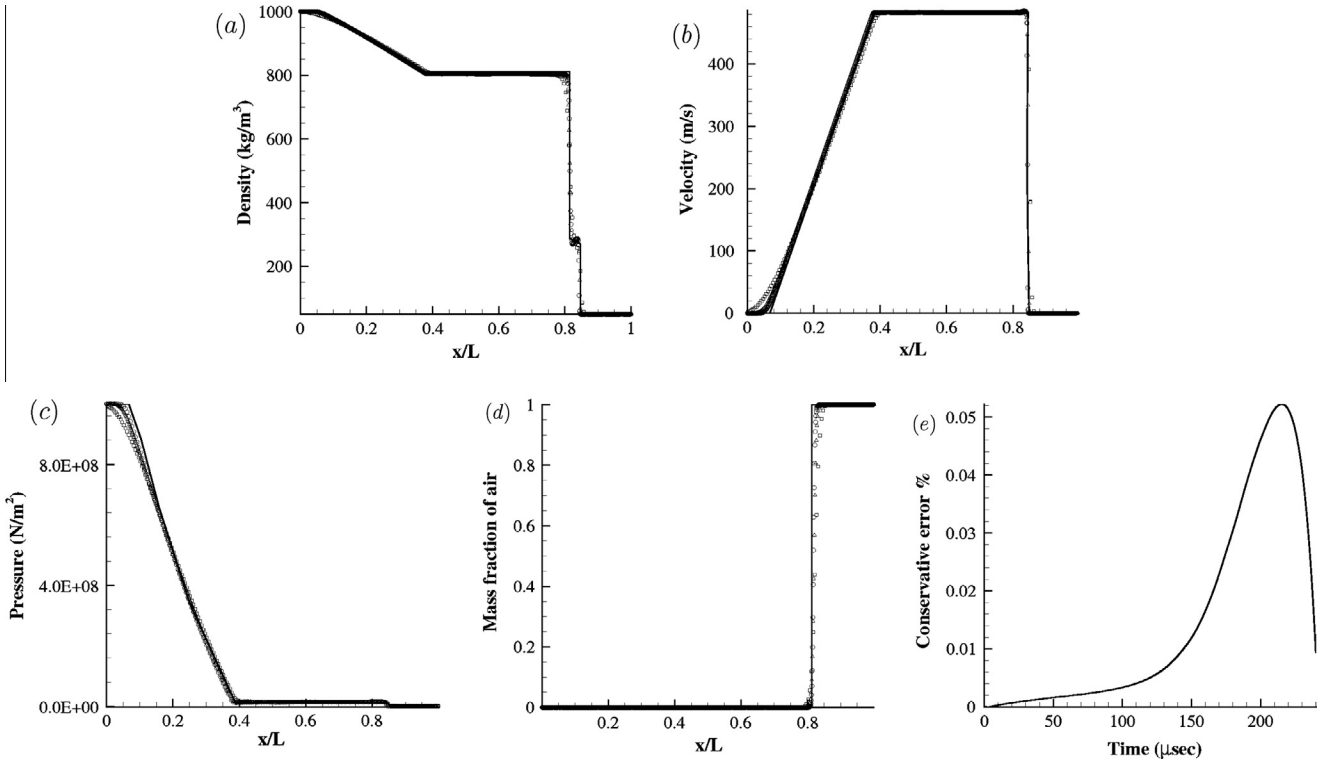

Fig. 6. Comparison of numerical and analytical results for (a) density, (b) velocity, (c) pressure and (d) mass fraction of air, ∘ : 1000 cells, △ : 500 cells, □: 200 cells, — : Analytical. (e) Conservation error percentage as a function of time.

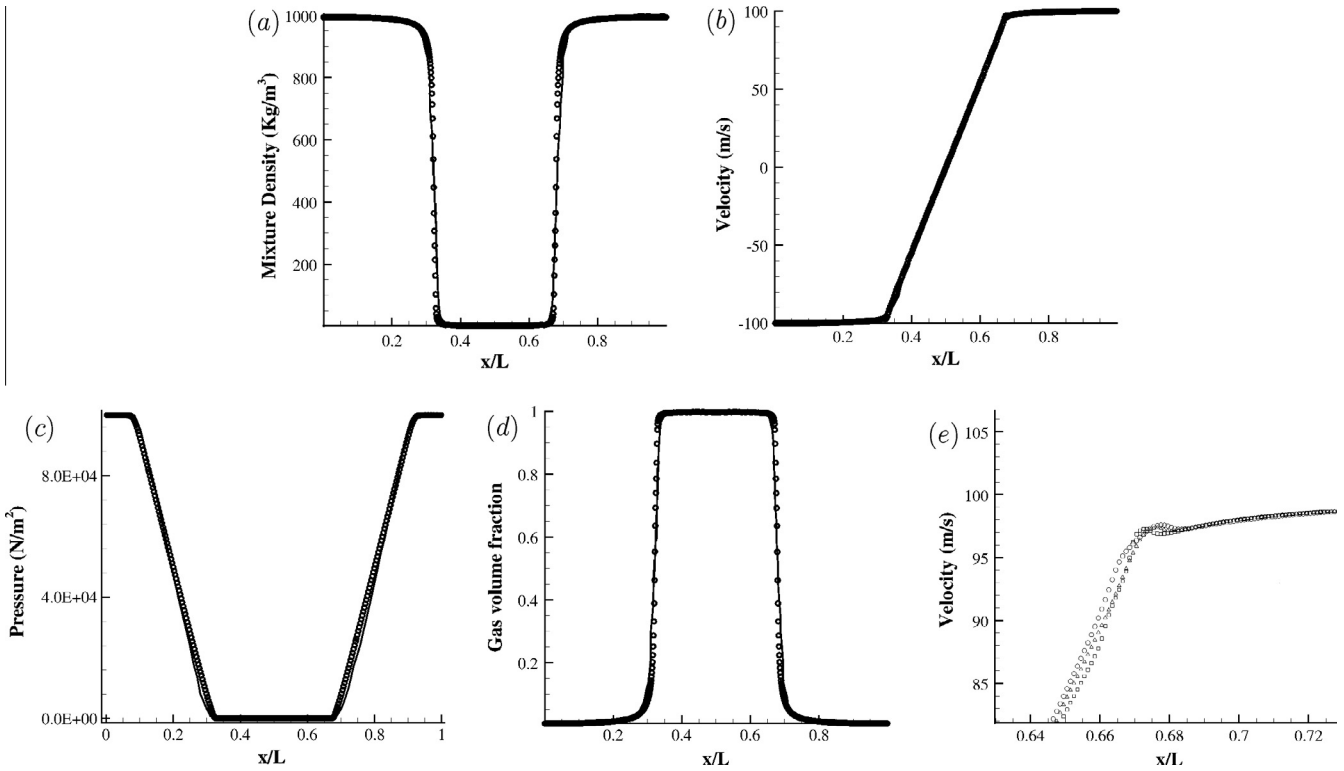

Fig. 7. Comparison of present numerical results and numerical results of Saurel and Lemetayer (2001) for (a) density, (b) velocity, (c) pressure and (d) volume fraction of vapor, ∘ : Present, — : Saurel and Lemetayer (2001). (e) Effect of k on velocity near a discontinuity, □: $k-2.0$, △: $k-4.0$, ○: $k-8.0$.

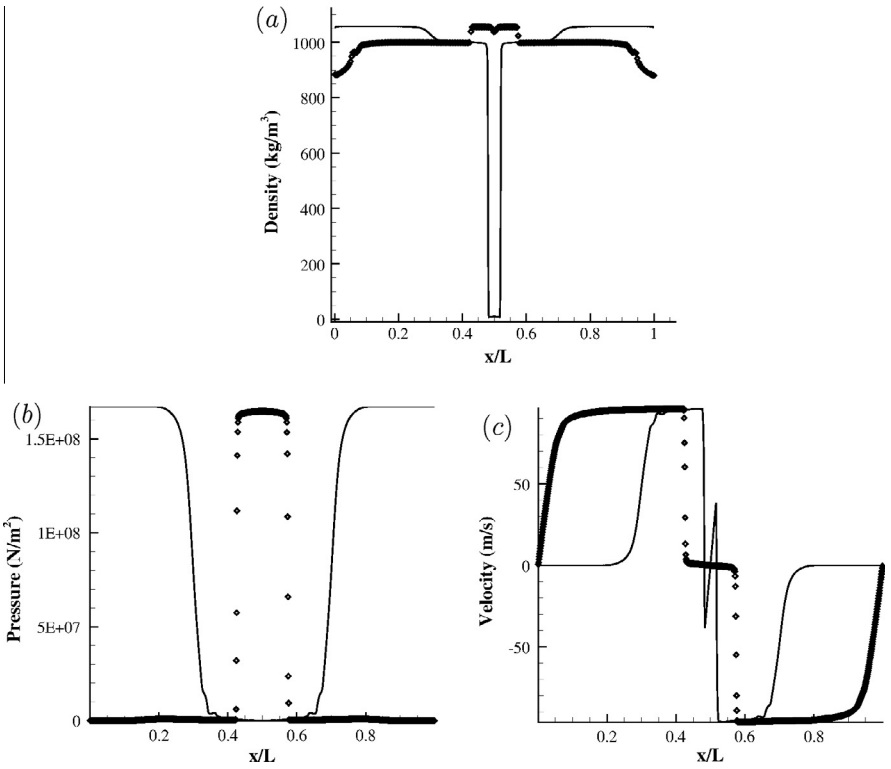

Fig. 8. Comparison of quantities before and after bubble collapse. (a) density, (b) pressure and (c) velocity, — : Before collapse, ♢ : After collapse.

This additional term prevents the switch from reaching very small values inside the cavitating vortex. Note that the additional term automatically goes to zero in single phase regions and hence termed as modified multiphase switch. Its effect is clearly seen in Fig. 4(b) in terms of an oscillation-free solution. Fig. 4(d) shows that the proposed modification prevents the switch from reaching very small

values inside the vortex. When applied to the turbulent problem discussed above, it yields identical results to the form proposed by Park and Mahesh (2007).

Results

We evaluate the proposed algorithm for a variety of flows. In Section 'Multiphase non cavitating shock tube', a multiphase shock tube problem is discussed. This problems helps in determining the accuracy of the shock capturing scheme in computing the jump conditions. In Sections 'One dimensional cavitating tube' and 'One dimensional reflecting-cavitating tube', one dimensional cavitating problems are discussed. Finally in Sections 'RANS of turbulent cavitating flow over a hydrofoil' and 'LES of turbulent cavitating flow over a wedge', the algorithm is validated for turbulent cavitating flows.

Multiphase non cavitating shock tube

A two phase shock tube with water and compressed air (Lagumbay et al., 2007; Abgrall and Karni, 2001) is simulated. We use this problem to demonstrate the advantage of the internal energy equation over the total energy equation in the predictor step. The driver section contains liquid water at high pressure, the driven section contains compressed air at lower pressure and the interface is present at $x/L = 0.7$ initially. The problem is stiff; the density and pressure differ by ratios of 20 and 10^4 respectively across the discontinuities. The computational domain is discretized uniformly using 1000 volumes and a time step of 1×10^{-8} s is used. The initial conditions are given by

$$\begin{aligned} Q &= [\rho, u, P, \gamma, Y], \\ Q_W &= [1000, 0, 1.5.10^9, 4.4, 0.0], \\ Q_A &= [50, 0, 1.0.10^5, 1.4, 1.0]. \end{aligned} \tag{38}$$

Fig. 5(a) shows a schematic of the problem and Figs. 5(b) and (c) show the temperature and pressure obtained at the material discontinuity at the end of the predictor step of the very first iteration. It clearly shows that internal energy equation is able to produce an oscillation-free solution while the total energy equation does not, for the same time step. This is because a primitive variable formulation is less prone to aliasing errors. Consider the pressure term in the total energy equation. This term $\frac{\partial (p u_j)}{\partial x_j}$ has a product inside the derivative and associated aliasing as opposed to the term $p \frac{\partial u_j}{\partial x_j}$ in the internal energy equation. Also a spatial derivative of a linear term (as in the internal energy equation) will be more accurate than that of a quadratic product (as in the total energy equation),

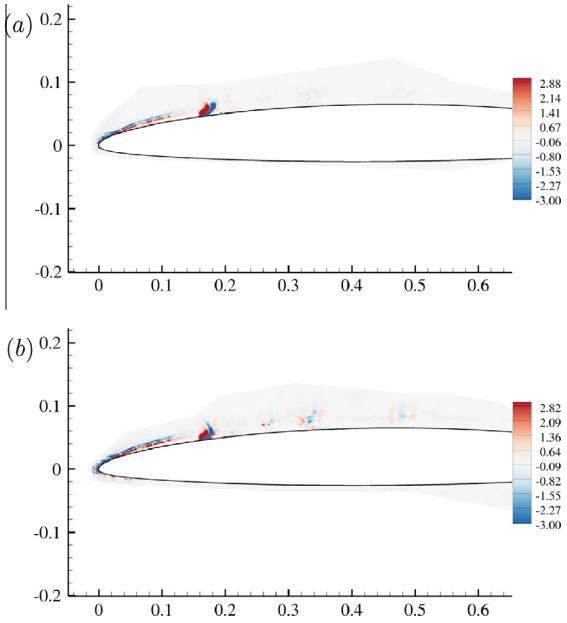

Fig. 10. Instantaneous dissipative flux for (a) continuity equation, (b) u-momentum equation.

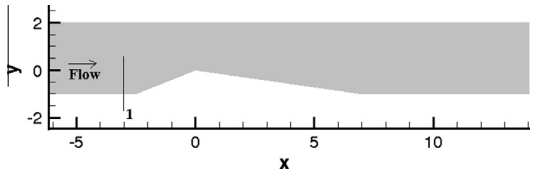

Fig. 11. Geometry and computational domain for wedge.

due to its lower spatial order. Further, Karni (1994) has demonstrated the effectiveness of using primitive variables in suppressing the pressure oscillations across a material discontinuity. Hence solving for internal energy which is a primitive variable helps in reducing these errors. However conservation errors will be large if a primitive variable is used to compute jump conditions. Hence the corrector step which computes the jump conditions uses total energy which is obtained at the end of the predictor step using Eq. (5). Fig. 6 shows the comparison between numerical and exact solution at 240 μs. Three different grids are used: 200, 500 and 1000 volumes. The solutions for all three grids agree with the

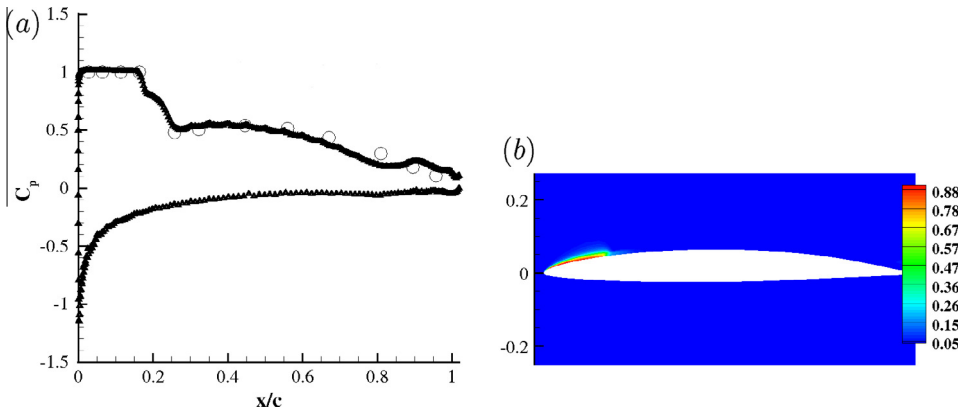

Fig. 9. (a) Comparison of pressure co-efficient (C_p) distribution to experiment, ○ : Shen and Dimotakis (1989), △ : Present. (b) Mean void fraction ($\overline{\alpha}$) contour for $\sigma = 1.0$.

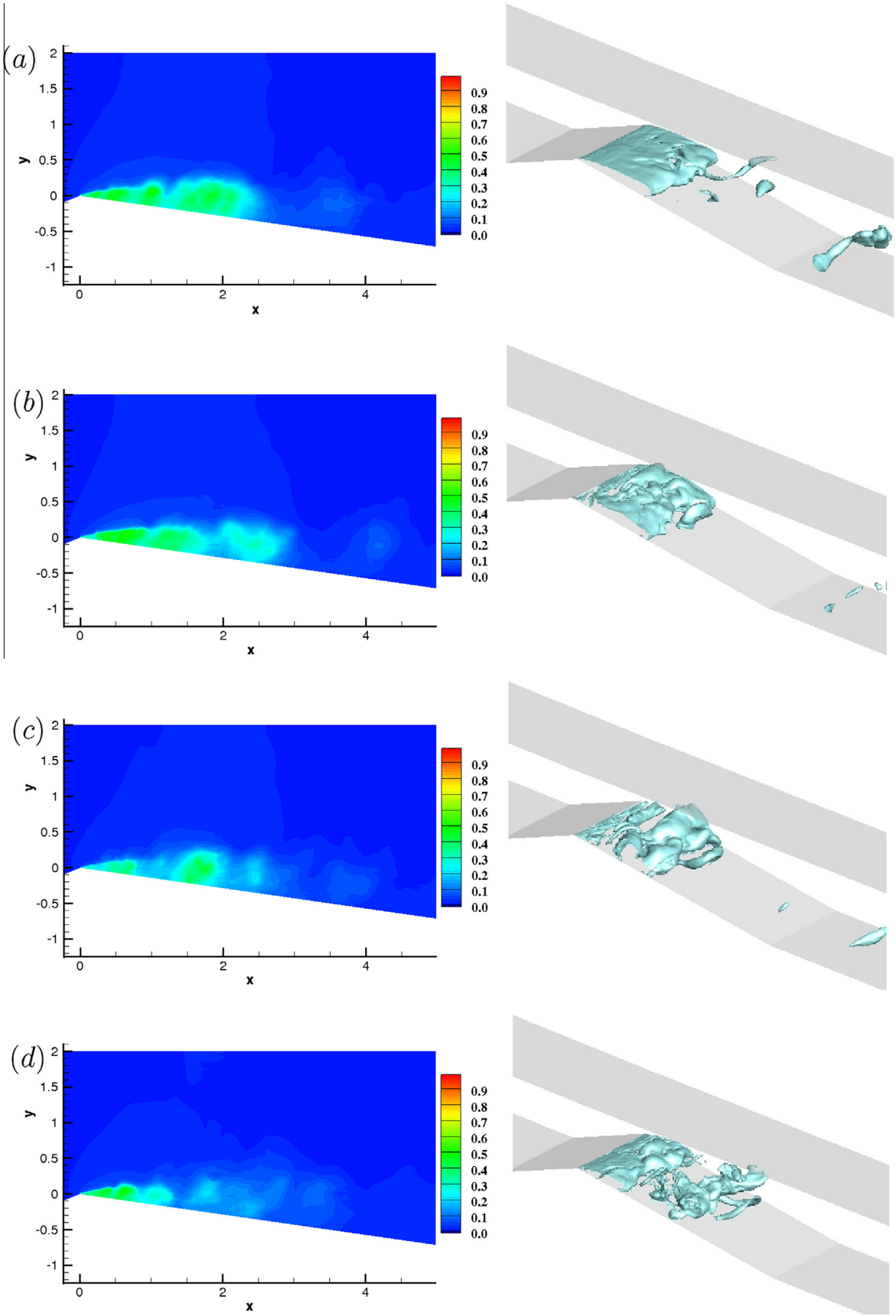

Fig. 12. Sequence of events leading to cavity destabilization, Left: Span averaged void fraction contour, Right: Isocontours of void fraction ($\alpha = 0.2$).

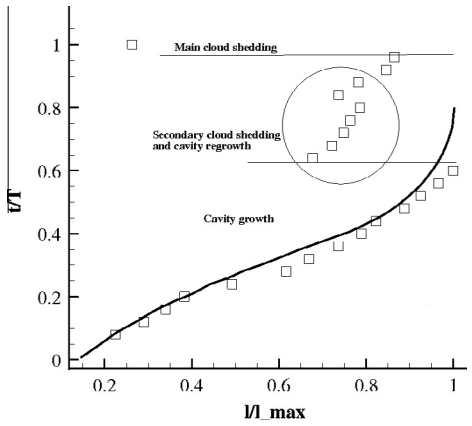

Fig. 13. Variation of non-dimensional cavity length with time in one cycle, — : Experimental fit (Callenaere et al., 2001), □: Present.

analytical results; improvement in accuracy with grid refinement can also be observed. The shock wave initially at $x/L = 0.7$ on interaction with the contact discontinuity, reflects as an expansion wave which travels in water. Fig. 6(e) shows that the usage of internal energy equation in the predictor step does not cause any significant conservation errors. The maximum conservative error obtained as $\frac{|\sum_V E_T - \sum_V E_{Tinitial}|}{\sum_V E_{Tinitial}}$ is found to be less than 1% for the finest grid.

One dimensional cavitating tube

This test problem involves a one dimensional tube consisting of water initially at atmospheric pressure and two streams moving away from the center at 100 m/s. The computational domain is discretized uniformly using 1000 volumes and a time step of 1×10^{-6} s is used. This problem has been previously investigated by many authors (Saurel and Lemetayer, 2001; Liu et al., 2004; Barberon and Helluy, 2005). We compare our results with the results obtained using a multi fluid approach by Saurel and Lemetayer (2001) in Fig. 7. The expansion at the center causes a vapor bubble to be produced as soon as the pressure reaches vapor pressure. Thus two interfaces are created dynamically due to the rarefaction waves. The mixture density, pressure, velocity and vapor volume fraction at the end of 1860 μs are compared with numerical results from Saurel and Lemetayer (2001) and the results agree very well with each other. Further, the effect of k, the adjustable parameter has been demonstrated. The velocity profile obtained using three different values of k (2, 4 and 8) is magnified near a discontinuity and plotted in Fig. 7(e). For lower values of k, small oscillations are observed which gets smoothed out at higher values. This is clearly the effect of increased dissipation. Apart from this, no other significant differences are observed.

One dimensional reflecting-cavitating tube

This case is similar to the previous problem but with the ends of the tube closed instantaneously at $t = 0$. This causes shock waves at the ends which propagate towards the center in addition to the rarefaction wave moving away from the center. This problem is used to demonstrate shock-bubble interaction and robustness of the method in handling bubble collapse. The computational domain is discretized uniformly using 1000 volumes and a time step of 1×10^{-8} s is used. The initial conditions are identical to the previous problem. Liu et al. (2004) have studied this problem although with a different equation of state. The end walls act as reflecting boundaries causing a shock at time $t = 0$ and a cavitation bubble is formed at the center due to the expansion. The shock wave and the rarefaction wave meet as they travel in opposite directions and after interaction continue to travel with a mitigated strength. Fig. 8 shows two instances of time, one before vapor bubble collapse and one after collapse. Before collapse, the vapor bubble can be clearly seen at the center. The shock wave on interaction with the interface leads to a stronger discontinuity in velocity and pressure. After collapse, the center of the tube is filled with water which can be seen from the density curve. The condensation waves travel outward from the center which is also clearly seen in the pressure curve. The results agree qualitatively with Liu et al. (2004), and also demonstrate that the numerical method is able to handle bubble collapse well.

RANS of turbulent cavitating flow over a hydrofoil

We consider a turbulent cavitating flow over a hydrofoil. Shen and Dimotakis (1989) conducted experiments on this hydrofoil and our numerical results are compared against their experimental results. The hydrofoil section used is NACA 66 (mod) with a camber ratio of 0.02 and a thickness ratio of 0.09. The Reynolds number based on chord length c is 2×10^6, the angle of attack is 4 degrees and the cavitation number $\sigma = \frac{p_\infty - p_v}{0.5\rho_\infty u_\infty^2}$ is 1.0. At this cavitation number, a leading edge cavity, also referred as partial sheet cavity/open cavity (Leroux et al., 2004; Laberteaux and Ceccio, 2001) is observed in the experiment. A streamwise grid spacing of 0.0005c is used near the stagnation region to capture cavitation

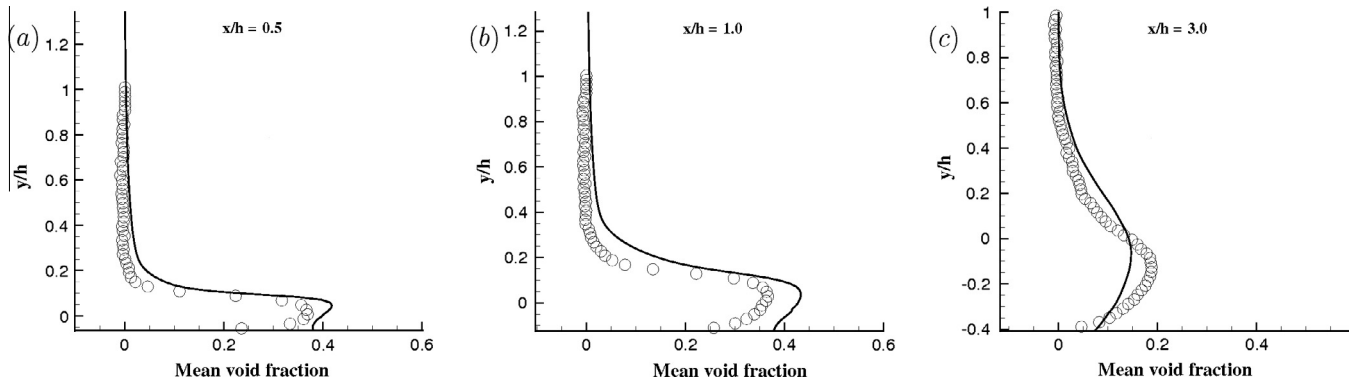

Fig. 14. Comparison of average volume fraction to experimental values at different streamwise locations, ○ : Experiment (Prof. Ceccio, private communication), — : Present.

inception and the wall normal spacing is 0.0008c. The governing equations Eq. (3) are Reynolds averaged giving rise to Reynolds stress terms, which are modeled using the Spalart–Allmaras eddy viscosity model (Spalart and Allmaras, 1992). Fig. 9(a) shows the time averaged pressure coefficient distribution along the chord for both the suction and pressure sides. The results are seen to agree well with the experimental results. Fig. 9(b) shows the mean void fraction contour showing the presence of a sheet cavity near the leading edge. This result also agrees with the conclusions of Leroux et al. (2004), that a quasi-stable partial sheet cavity is formed for cavity lengths less than half the chord length.

As discussed in the introduction section, localization of dissipation is essential to accurately simulate turbulent flows. To assess this effect, the filter flux $\frac{F^*_{fc}}{V_{cv}}$ is computed and plotted separately for both continuity and u-momentum equations alone for the purpose of illustration, where $F^*_{fc} = \frac{1}{2} R_{fc} \Phi^*_{fc}$. Fig. 10(a) clearly shows that the filter fluxes are active only near the cavity inception and cavity closure locations where the density gradient is maximum. Similar trends can be observed even in the u-momentum equation in Fig. 10(b). Further, small values of filter flux are seen in the cavitating vortices that are shed from the cavity closure. This behavior shows that the dissipation is localized to the vicinity of discontinuities.

LES of turbulent cavitating flow over a wedge

Next, we consider LES of sheet to cloud cavitation over a wedge. The Reynolds number based on the maximum wedge height ($h = 1$ in.) and a bulk velocity of 7.9 m/s is approximately 0.2×10^6. The domain is extended both upstream (up to a length of $20h$) and downstream (up to a length of $40h$) of the wedge, and sponge boundary conditions are used to minimize reflections from the boundaries. No slip boundary conditions are imposed on top and bottom walls. Periodic boundary conditions are enforced in the spanwise boundaries. Fig. 11 shows the geometry of the wedge considered. The upstream cavitation number at the station marked as 1 in Fig. 11 is 2.0. Velocity, pressure and density are specified at the inflow to obtain the correct experimental conditions at Station 1. An exit pressure is specified while other quantities at the outflow are extrapolated from the interior of the domain. The minimum near wall spacing is $0.002h$ in both normal and streamwise directions near the wedge. The span is discretized uniformly using 80 cells. The sequence of events leading to sheet to cloud cavitation is depicted in Fig. 12. The left hand side figures show the span averaged void fraction contours while the right hand side figures show three dimensional isocontours of void fraction. A fully formed cavity first develops up to a length $x/h = 2.6$, where h is the height of the wedge (Fig. 12(a)). It then pinches off close to the trailing edge, shedding a small secondary cloud (Fig. 12(b)). The main cavity then pinches off close to the leading edge, and finally a new sheet cavity starts to form (Fig. 12(c) and (d)).

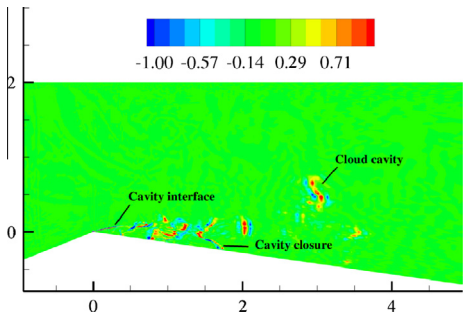

Fig. 15. Dissipative flux showing localization near cavity interface, closure and inside cloud cavity.

The Strouhal number corresponding to this behavior $St = \frac{f l_{max}}{U_{inf}}$ is computed to be 0.28, which lies within the acceptable range of 0.25–0.4 (Callenaere et al., 2001). Here, l_{max} is the maximum mean length of the cavity and U_{inf} is the free stream velocity just before the apex of the wedge. The cavity length obtained at various time instances is compared with experimental data of Callenaere et al. (2001) in Fig. 13. Here, the length of the cavity (l) plotted along the abscissa is normalized using the maximum cavity length ($l_{max}/h = 2.6$) and the time (t) is normalized using the time period of the entire cycle (T), which is about 21 ms for this case. The sheet cavity grows up to its maximum length until about $0.65T$. A small secondary cloud is then shed, which is not normally captured in RANS simulations (Seo and Lele, 2009). Leroux et al. (2004) have observed such secondary cloud shedding also in a hydrofoil geometry. After a small period of cavity regrowth, an abrupt change in cavity length is observed when the cloud pinches off from the main cavity at $l/l_{max} = 0.3$.

The mean volume fraction values at three different streamwise locations are compared with X-ray measurements from experiments (Ganesh and Ceccio, personal communication) in Fig. 14 and a reasonable agreement is obtained. The simulations slightly overpredict the maximum void fraction value at the first two locations, but the shape of the cavity is predicted well. At the third location near the cavity closure the simulations slightly underpredict the maximum void fraction value. Fig. 15 shows the dissipative flux in the continuity equation, to illustrate localization of dissipative flux. It can be observed that the dissipation is significant only at the cavity interface, cavity closure and inside the cloud cavity. The dissipative fluxes for other equations also show similar behavior and hence are not shown here.

Summary

A numerical method is developed to simulate multiphase cavitating flows. A homogeneous mixture model is used to model the multiphase mixture as a single compressible fluid. The internal energy form of energy equation is used and is shown to discretely outperform the total energy form. A characteristic-based filter is developed to handle shocks and material discontinuities. A predictor corrector method is adopted where the predictor step is non-dissipative and the corrector step is independent of the base scheme in the predictor step. A sensor based on vorticity, divergence and volume fraction is used in the corrector step to prevent excessive dissipation away from the discontinuities. The method is first validated for canonical one dimensional problems and the accuracy of the shock capturing scheme is demonstrated. The method is then applied to study two turbulent cavitating flows using both RANS and LES methodologies. The cases represent two different types of cavitation namely leading edge cavitation and sheet to cloud cavitation. Good agreement with experimental results is demonstrated for both the cases and it is shown that the method can be used with both RANS and LES methodologies.

Acknowledgments

This work is supported by the United States Office of Naval Research under Grant ONR N00014-11-1-0497 with Dr. Ki-Han Kim as the program manager. Computing resources were provided by the Arctic Region Supercomputing Center of HPCMP and the Minnesota Supercomputing Institute. The authors also thank Prof. Steven Ceccio, University of Michigan for providing the experimental data.

References

Abgrall, R., Karni, S., 2001. Computations of compressible multifluids. J. Comput. Phys. 169, 594–623.

Adams, N.A., Schmidt, S.J., 2013. Shocks in cavitating flows. In: Bubble Dynamics and Shock Waves. Springer, pp. 235–256.

Ahuja, V., Hosangadi, A., Arunajatesan, S., 2001. Simulations of cavitating flows using hybrid unstructured meshes. J. Fluids Eng. 123, 331–340.

Arndt, R.E., Song, C., Kjeldsen, M., He, J., Keller, A., 2000. Instability of partial cavitation: a numerical/experimental approach. In: Twenty Third Symposium on Naval Hydrodynamics.

Barberon, T., Helluy, P., 2005. Finite volume simulation of cavitating flows. Comput. Fluids 34, 832–858.

Bensow, R.E., Bark, G., 2010. Implicit LES predictions of the cavitating flow on a propeller. J. Fluids Eng. 132, 041302.

Callenaere, M., Franc, J.-P., Michel, J., Riondet, M., 2001. The cavitation instability induced by the development of a re-entrant jet. J. Fluid Mech. 444, 223–256.

Dittakavi, N., Chunekar, A., Frankel, S., 2010. Large eddy simulation of turbulent-cavitation interactions in a Venturi nozzle. J. Fluids Eng. 132, 121301.

Ducros, F., Ferrand, V., Nicoud, F., Weber, C., Darracq, D., Gacherieu, C., Poinsot, T., 1999. Large-eddy simulation of the shock/turbulence interaction. J. Comput. Phys. 152, 517–549.

Frikha, S., Coutier-Delgosha, O., Astolfi, J.-A., 2008. Influence of the cavitation model on the simulation of cloud cavitation on 2D foil section. Int. J. Rotating Machinery.

Germano, M., Piomelli, U., Moin, P., Cabot, W.H., 1991. A dynamic subgrid-scale eddy viscosity model. Phys. Fluids A: Fluid Dynam. (1989–1993) 3, 1760–1765.

Goncalvès, E., Patella, R.F., 2010. Numerical study of cavitating flows with thermodynamic effect. Comput. Fluids 39, 99–113.

Gustafsson, B., Olsson, P., 1995. Fourth-order difference methods for hyperbolic IBVPs. J. Comput. Phys. 117, 300–317.

Harten, A., 1983. High resolution schemes for hyperbolic conservation laws. J. Comput. Phys. 49, 357–393.

Henry, R.E., Grolmes, M., Fauske, H.K., 1971. Pressure-pulse propagation in two-phase one-and two-component mixtures. Tech. Rep., Argonne National Lab., Ill.

Hosangadi, A., Ahuja, V., 2005. Numerical study of cavitation in cryogenic fluids. J. Fluids Eng. 127, 267–281.

Hou, Y., Mahesh, K., 2005. A robust, colocated, implicit algorithm for direct numerical simulation of compressible, turbulent flows. J. Comput. Phys. 205, 205–221.

Ji, B., Luo, X.-w., Peng, X.-x., Wu, Y.-l., 2013. Three-dimensional large eddy simulation and vorticity analysis of unsteady cavitating flow around a twisted hydrofoil. J. Hydrodynam., Ser. B 25, 510–519.

Karni, S., 1994. Multicomponent flow calculations by a consistent primitive algorithm. J. Comput. Phys. 112, 31–43.

Karplus, H.B., 1957. Velocity of sound in a liquid containing gas bubbles. J. Acoust. Soc. Am. 29, 1261.

Kinzel, M.P., Lindau, J.W., Peltier, L.J., Kunz, R.F., Sankaran, V., 2007. Detached-eddy simulations for cavitating flows. AIAA Paper (2007-4098).

Kunz, R.F., Boger, D.A., Stinebring, D.R., Chyczewski, T.S., Lindau, J.W., Gibeling, H.J., Venkateswaran, S., Govindan, T., 2000. A preconditioned Navier–Stokes method for two-phase flows with application to cavitation prediction. Comput. Fluids 29, 849–875.

Laberteaux, K., Ceccio, S., 2001. Partial cavity flows. Part 1. Cavities forming on models without spanwise variation. J. Fluid Mech. 431, 1–41.

Lagumbay, R.S., Vasilyev, O.V., Haselbacher, A., 2007. Homogeneous equilibrium mixture model for simulation of multiphase/multicomponent flows. Int. J. Numer. Methods Fluids 4, 1–6.

Leroux, J.-B., Astolfi, J.A., Billard, J.Y., 2004. An experimental study of unsteady partial cavitation. J. Fluids Eng. 126, 94–101.

Liu, T., Khoo, B., Xie, W., 2004. Isentropic one-fluid modelling of unsteady cavitating flow. J. Comput. Phys. 201, 80–108.

Lo, S.-C., Blaisdell, G., Lyrintzis, A., 2010. High-order shock capturing schemes for turbulence calculations. Int. J. Numer. Methods Fluids 62, 473–498.

Mahesh, K., Constantinescu, G., Moin, P., 2004. A numerical method for large-eddy simulation in complex geometries. J. Comput. Phys. 197, 215–240.

Park, N., Mahesh, K., 2007. Numerical and modeling issues in LES of compressible turbulence on unstructured grids. AIAA 2007 722.

Saito, Y., Takami, R., Nakamori, I., Ikohagi, T., 2007. Numerical analysis of unsteady behavior of cloud cavitation around a NACA 0015 foil. Comput. Mech. 40, 85–96.

Saurel, R., Lemetayer, O., 2001. A multiphase model for compressible flows with interfaces, shocks, detonation waves and cavitation. J. Fluid Mech. 431, 239–271.

Schmidt, S., Schnerr, G., Thalhamer, M., 2009. Inertia controlled instability and small scale structures of sheet and cloud cavitation. In: Seventh International Symposium on Cavitation.

Schnerr, G.H., Sezal, I.H., Schmidt, S.J., 2008. Numerical investigation of three-dimensional cloud cavitation with special emphasis on collapse induced shock dynamics. Phys. Fluids 20, 040703.

Semenov, N., Kosterin, S., 1964. Results of studying the speed of sound in moving gas-liquid systems. Teploenergetika 11, 46–51.

Senocak, I., Shyy, W., 2002. A pressure-based method for turbulent cavitating flow computations. J. Comput. Phys. 176, 363–383.

Seo, J., Lele, S., 23009. Numerical investigation of cloud cavitation and cavitation noise on a hydrofoil section. In: Seventh International Symposium on Cavitation.

Seo, J.H., Moon, Y.J., Shin, B.R., 2008. Prediction of cavitating flow noise by direct numerical simulation. J. Comput. Phys. 227, 6511–6531.

Shen, Y., Dimotakis, P.E., 1989. The influence of surface cavitation on hydrodynamic forces. In: 2nd American Towing Tank Conference.

Shin, B., Iwata, Y., Ikohagi, T., 2003. Numerical simulation of unsteady cavitating flows using a homogenous equilibrium model. Computat. Mech. 30, 388–395.

Singhal, A.K., Athavale, M.M., Li, H., Jiang, Y., 2002. Mathematical basis and validation of the full cavitation model. J. Fluids Eng. 124, 617–624.

Spalart, P.R., Allmaras, S.R., 1992. A one equation turbulence model for aerodynamic flows. AIAA J. 94, 1–22.

Wang, G., Ostoja-Starzewski, M., 2007. Large eddy simulation of a sheet/cloud cavitation on a NACA0015 hydrofoil. Appl. Math. Modell. 31, 417–447.

Yee, H.C., Sandham, N.D., Djomehri, M., 1999. Low-dissipative high-order shock-capturing methods using characteristic-based filters. J. Comput. Phys. 150, 199–238.

Zhang, X., Qiu, L., Gao, Y., Zhang, X., 2008. Computational fluid dynamic study on cavitation in liquid nitrogen. Cryogenics 48, 432–438.